Article ID: 1000-324X(2023)09-1110-07 **DOI:** 10.15541/jim20220756

Comparison of Hybrid Functionals HSE and PBE0 in Calculating the Defect Properties of $CsPbI_3$

WU Xiaowei[1], ZHANG Han[1,2], ZENG Biao[1,2], MING Chen[1,2], SUN Yiyang[1,2]

(1. Shanghai Institute of Ceramics, Chinese Academy of Sciences, Shanghai 201899, China; 2. Center of Materials Science and Optoelectronics Engineering, University of Chinese Academy of Sciences, Beijing 100049, China)

Abstract: Density functional theory calculations play an important role in the study of defects in halide perovskites. Although the traditional semi-local functionals (such as PBE) can obtain the band gaps close to the experiments, they fail to accurately describe the positions of the band edges. Utilizing more accurate hybrid functionals combined with the spin-orbit coupling (SOC) effect with full structure relaxation is considered to be necessary for the prediction of defect properties. There are two types of hybrid functionals in the literature, namely the screened HSE and the unscreened PBE0. In this study, taking the orthorhombic phase $CsPbI_3$ as an example, these methods were compared for the calculation of defect properties. The results show that there is no obvious difference between two methods for bulk properties, but qualitative differences appear for the defect properties. Most of the shallow-level defects predicted in the HSE calculations become deep-level defects in the PBE0 calculations. Meanwhile, there are qualitative differences between the defect transition levels and the Kohn-Sham levels. The origin of above differences lies in the fact that the Hartree-Fock exchange potential has long-range interaction. Therefore, in unscreened hybrid functionals, such as PBE0, it is more difficult to obtain convergent results with a manageable supercell size. In contrast, HSE exhibits a screening effect on the Hartree-Fock exchange potential and can obtain accurate defect energy levels using relatively small supercell sizes. Therefore, all results here demonstrate that the HSE hybrid functional owns a significant advantage in dealing with this problem even though a large Hartree-Fock mixing parameter (about 0.43) is needed.

Key words: perovskites; intrinsic defect; $CsPbI_3$; hybrid functional; first-principles calculation

Over the past decade, halide perovskite materials, represented by $CH_3NH_3PbI_3$, have made significant progress in the field of new solar cell materials. These materials do not contain any rare elements, and can be fabricated by low-cost methods[1-6]. In 2009, Miyasaka group[7] achieved a photoelectric conversion efficiency of 3.8%. In 2013, Grätzel and Snaith group[2,8] achieved an efficiency of 15% using different cell structures. Recently, the highest efficiency of perovskite solar cells verified by the US National Renewable Energy Laboratory has reached 25.7%, which is close to the record of silicon-based cells (26.7%)[9]. Currently, halide perovskite solar cells still face some urgent problems, including material stability, lead toxicity, and efficiency reduction in large-scale cells. Despite These problems, the ability of halide perovskite solar cells to achieve such high efficiency in a short period of time is still unprecedented in the history of solar cell development.

The halide perovskite materials also exhibit promising properties as luminescent materials. Research on the luminescence properties of these materials dates back to 1977[10]. In 1994, the first organic-inorganic hybrid layered halide perovskite-based light-emitting diode (LED) was reported[11]. In 2014, with the significant progress in perovskite photovoltaics, an infrared LED based on $CH_3NH_3PbI_3$ was achieved at room temperature[12]. In 2018, quantum efficiencies higher than 20% were achieved in perovskite infrared and green LEDs through submicron structural design and compositional engineering[13-14]. Moreover, halide perovskite materials have also received

Received date: 2022-12-17; **Revised date:** 2023-05-11; **Published online:** 2023-06-01
Foundation item: National Key R&D Program of China (2021YFB3500501)
Biography: WU Xiaowei (1993–), female, Master. E-mail: wxw_xiaowei@163.com
吴晓维(1993–), 女, 硕士. E-mail: wxw_xiaowei@163.com
Corresponding author: SUN Yiyang, professor. E-mail: yysun@mail.sic.ac.cn
孙宜阳, 研究员. E-mail: yysun@mail.sic.ac.cn

widespread attentions in fields such as light detection and high-energy particle detection[15-17].

It is worthwhile noting that these materials with excellent properties can be prepared by a relatively inexpensive solution method. Such synthesis method may introduce a substantial number of defects into halide perovskites. The development of traditional semiconductor materials is often limited by the control on defects, whereas halide perovskite materials exhibit high degree of tolerance to defects[18-25]. Theoretical calculations based on first-principles also support this view. For example, computational studies of $CH_3NH_3PbI_3$ have found that the intrinsic defects tend to form shallow energy levels, which do not significantly contribute to carrier recombination. Deep energy levels in these materials are typically associated with Pb dimers or I trimers, which tend to occur only when the Fermi level is close to the band edges[26-27]. Therefore, in halide perovskite materials, which are commonly insulators (*i.e.*, having the Fermi level near the center of the bandgap), defects with deep energy level may not appear.

First-principles calculations based on density functional theory (DFT) are the main method to study the properties of point defects in semiconductor materials. Hybrid functionals have become a frequently used method in the study of point defects in semiconductor materials due to their accurate treatment of band gap. Combined with the spin-orbit coupling (SOC) effect, hybrid functionals can obtain band gaps that agree with experimental measurements[25]. However, to obtain band gaps that are consistent with experiments, parameters controlling the Hartree-Fock exchange energy ratio (denoted as α) need to be adjusted. Typically, α is set to 0.43 for the screened hybrid functional HSE calculations, and α is set to around 0.2 for the unscreened hybrid functional PBE0 calculations[28-36]. The results obtained from these two methods have been discussed in bulk property calculations[37]. Their difference in defect calculations has also been reported for the organic-inorganic hybrid perovskite materials[38]. However, due to the uncertainty of structures of the organic cations at 0 K, the mechanism behind this difference remains unclear.

In recent years, pure inorganic halide perovskite materials that do not contain organic cations (such as $CH_3NH_3^+$ and $NH_2CHNH_2^+$) have rapidly developed[39-46]. They not only possess higher thermodynamic stability but also avoid the potential volatility of organic cations[47-48]. Among pure inorganic halide perovskite materials, $CsPbI_3$ has a suitable band gap for the preparation of solar cells, and the efficiency of this material has exceeded 21%[49]. In this study, the defect transition levels (DTL) of all point defects for $CsPbI_3$ calculated by HSE-0.43 and PBE0-0.2 functionals were compared to determine the effective method to accurately calculate the defect properties of halide perovskite.

1　Computation method

The VASP package was used in this work [50] and the orthorhombic phase of $CsPbI_3$ (*i.e.*, γ-$CsPbI_3$) was considered. The interaction between ions and valence electrons was described by PAW potentials[51-52]. In calculations a plane-wave basis set was used, and changes in the volume or shape of the cell were considered. The plane-wave cutoff energy was set to 408 eV (approximately 30 Ry) for calculations with varying cell parameters, and 238 eV for calculations with fixed cell parameters. The screened hybrid functional HSE and the unscreened hybrid functional PBE0 were compared. As mentioned above, the Hartree-Fock exchange energy mixing parameter α was set to 0.43 (denoted as HSE-0.43) in the HSE calculation, while it was set to 0.2 (denoted as PBE0-0.2) in the PBE0 calculation. Except for the cell parameter optimization, all calculations included the SOC effect.

The equilibrium volume of the primitive cell was obtained by fitting the Murnaghan equation of state. The fitting used nine data points distributed uniformly within ±12% of the equilibrium volume. For structural optimization of each data point, the lattice constants are allowed to vary while the cell volume was fixed. The bulk modulus of the material can also be obtained from the fitting of the equation of state. After obtaining the equilibrium volume through fitting, the parameters of the primitive cell and internal structural parameters were further optimized. The convergence criteria for total energy and forces were set to 1.36×10^{-7} eV and 5.14×10^{-2} eV/nm (approximately 2×10^{-4} Ry/Bohr), respectively. The Brillouin zone was sampled using a 3×2×3 *k*-grid centered at the Γ point.

The band structure calculations were performed using the 3×2×3 *k*-grid amended with the *k*-points on the high-symmetry paths, whose weights were set to zero. The effective masses were obtained by parabolic fitting of the bands near the Γ point using six data points (including Γ). The density of states and dielectric constant were calculated using a 5×4×5 *k*-grid and 720 bands which contain 544 valence bands. It was found that the choices of *k*-grid (3×2×3 or 5×4×5) and plane wave cutoff energies (408 or 238 eV) have insignificant effects on the band gap width (<0.01 eV).

Defect calculations were performed using the supercell method. A supercell containing 160 atoms was constructed from a primitive cell of 20 atoms using a

transformation matrix (2 0 0 | 0 1 -1 | 0 2 2). The Brillouin zone of the supercell was represented by the Γ point. Structural relaxations were carried out using hybrid functionals combined with the SOC effect until the forces on all atoms were less than 0.257 eV/nm. To perform batch calculations using hybrid functional combined with the SOC effect, the PREC and PRECFOCK parameters were set to Normal and Fast, respectively. The DTL calculation was performed using the formula

$$\varepsilon(q/q') = \frac{E_{\mathrm{D}}^{q} - E_{\mathrm{D}}^{q'}}{q' - q} - E_{\mathrm{VBM}} \quad (1)$$

where E_{D}^{q} and $E_{\mathrm{D}}^{q'}$ represent the total energy of point defects with charge state q and q', respectively, and E_{VBM} is the Kohn-Sham eigenvalue at the valence band maximum of defect-free γ-$CsPbI_3$. Further details on the defect calculation method can be found in references[27, 53].

2 Results and discussion

Fig. 1 shows the E-V relationship between the unit cell volume and total energy. The data points are obtained from hybrid functional calculations without the SOC effects, and the curve represents the result fitted by the Murnaghan equation of state. It can be seen that the curves obtained by two functionals, HSE-0.43 and PBE0-0.2, are similar, and the fitted bulk modulus (B_0) values are 14.1 and 13.3 GPa, respectively, indicating that $CsPbI_3$ is a soft material.

Based on the equilibrium volume obtained by fitting the Murnaghan equation of state, primitive cell optimization was performed, and it was found that the lattice constants obtained by PBE0-0.2 are slightly larger than those obtained by HSE-0.43, as shown in Table 1. The differences in internal structural parameters obtained by two methods are less than 0.2%.

Fig. 2 compares the band structures obtained by two

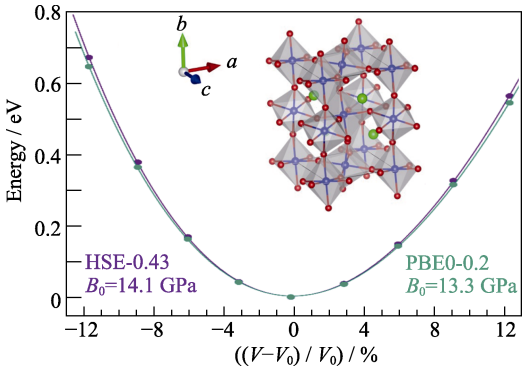

Fig. 1 Fitting Murnaghan equation of state to obtain the equilibrium volume and bulk modulus with inset showing the atomic structure of γ-phase $CsPbI_3$

methods. Since the calculations combining hybrid functionals and SOC require high computational cost, only energy bands along the three main axes from the Γ point were considered. The direct band gap at the Γ point obtained by HSE-0.43 and PBE0-0.2 are 1.71 and 1.68 eV, respectively. The band structures obtained by two methods are similar, with the main difference being that the valence band width obtained by HSE-0.43 (about 4.2 eV) is broader than that obtained by PBE0-0.2 (about 3.8 eV).

Fig. S1 in the supporting materials compares the density of states (DOS) obtained by two methods. Except for the smaller valence band width obtained by PBE0-0.2, there are no other significant differences. Fig. S2 compares the effective masses calculated by two methods. The electron effective masses obtained by HSE-0.43 are $(0.17–0.19)m_0$, while the hole effective masses are $(0.20–0.23)m_0$. The corresponding values obtained by PBE0-0.2 differ from the HSE-0.43 results by less than $0.1m_0$. Fig. S3 shows the real (ε_1) and imaginary (ε_2) parts of the dielectric constant. There is a slight difference in the bulk dielectric constant calculated by the HSE-0.43 and PBE0-0.2 functionals. At 0 eV, ε_1 is 4.4 and 4.6 from HSE-0.43 and PBE0-0.2, respectively. The slight shift of ε_2 obtained by the two methods is related to the slight difference in the band gaps.

Next, the differences between two methods in defect property calculations are discussed. In this study, vacancies of Cs, Pb, and I atoms (v_{Cs}, v_{Pb}, and v_{I}), interstitial atoms (Cs_i, Pb_i, and I_i), and anti-site defects ($\mathrm{Cs_{Pb}}$, $\mathrm{Pb_{Cs}}$, $\mathrm{Cs_I}$, $\mathrm{I_{Cs}}$, $\mathrm{Pb_I}$, and $\mathrm{I_{Pb}}$) are considered. As shown in Table 1, there are two symmetric positions for I atoms in the orthorhombic phase $CsPbI_3$, denoted as I_1 and I_2. Both positions were considered for defect calculations, and the one with lower energy were chosen to show the results.

We focus on shallow-level defects in this work. For deep-level defects, their positions in the band gap are affected by the interaction between periodic image charges, which is not the topic of discussion in this work.

Table 1 Lattice constants and internal parameters of orthorhombic $CsPbI_3$ calculated by two different hybrid functionals

	HSE-0.43			PBE0-0.20		
	X/*a*	*Y*/*b*	*Z*/*c*	*X*/*a*	*Y*/*b*	*Z*/*c*
	a/nm 0.9008	*b*/nm 1.2525	*c*/nm 0.8632	*a*/nm 0.9061	*b*/nm 1.2589	*c*/nm 0.8674
Cs	0.4312	0.25	0.0228	0.4294	0.25	0.0238
Pb	0	0	0	0	0	0
I_1	0.5110	0.25	0.5783	0.5104	0.25	0.5804
I_2	0.2021	0.0387	0.3017	0.2017	0.0395	0.3021

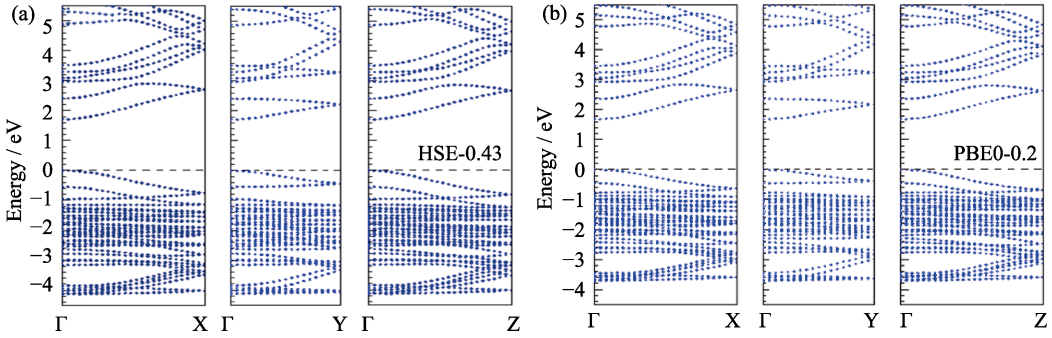

Fig. 2　Band structures of γ-$CsPbI_3$ calculated by two hybrid functionals HSE-0.43 (a) and PBE0-0.2 (b) including the SOC effect

Previous studies have found that deep-level defects in $CsPbI_3$ are often accompanied by the formation of Pb dimers and I trimers[26-27]. Therefore, the defect structures without the above-mentioned structural distortions were discussed, even if the structure is metastable. Fig. 3 shows the structures of intrinsic defects in neutral charge state, where no Pb dimers and I trimers appear. Since the defect structures obtained by two methods are similar, only the structures after relaxation with PBE-0.2 are shown in Fig. 3.

Fig. 4(a) shows the DTLs obtained by the HSE-0.43 functional for each defect. We only consider the transition from −1 to 0, $\varepsilon(-/0)$, for the acceptors and from 0 to +1, $\varepsilon(0/+)$, for the donors, as these two transition levels are most directly related to the nonradiative recombination of charge carriers[53]. As can be seen, in the absence of Pb dimers and I trimers, DTLs calculated by HSE-0.43 are all shallow-level defects, except for the slightly deep $\varepsilon(-/0)$ level of I_i. Fig. 4(b) shows DTLs calculated by the PBE0-0.2 hybrid functional, which exhibit a clear contrast with the results of HSE-0.43. Firstly, $\varepsilon(-/0)$ levels of all acceptor defects are significantly deeper, and $\varepsilon(0/+)$ levels of all donor defects except for Pb_i and Pb_I are also deeper.

To investigate the deep-level defects observed in the PBE0-0.2 calculation, Kohn-Sham levels of defect supercells obtained from two functionals were further compared. Six types of single acceptor and single donor defects with an unpaired electron (or hole) in their neutral state were selected, and the qualitative differences between the results of two functionals were clearly observed by examining the position of the unpaired electron (or hole) in Kohn-Sham energy levels. For the donor (or acceptor) defects, Fig. 5(a) shows the position of the unpaired electron (or hole) in the bandgap obtained from the HSE-0.43 calculation. For the typical shallow-level defects v_{Cs}, v_I, Cs_i, and Cs_{Pb}, the position of the unpaired electron (or hole) in the bandgap is very close to the band edge (*i.e.*, VBM or CBM). However, for the PBE0-0.2 results in Fig. 5(b), the energy level positions

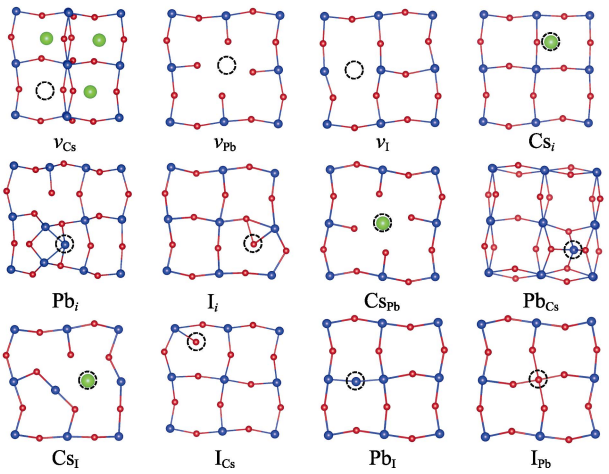

Fig. 3　Atomic structures of 12 intrinsic defects after relaxation in neutral charge state

As two functionals yield similar structures, only the structures from PBE0-0.2 calculations are shown here

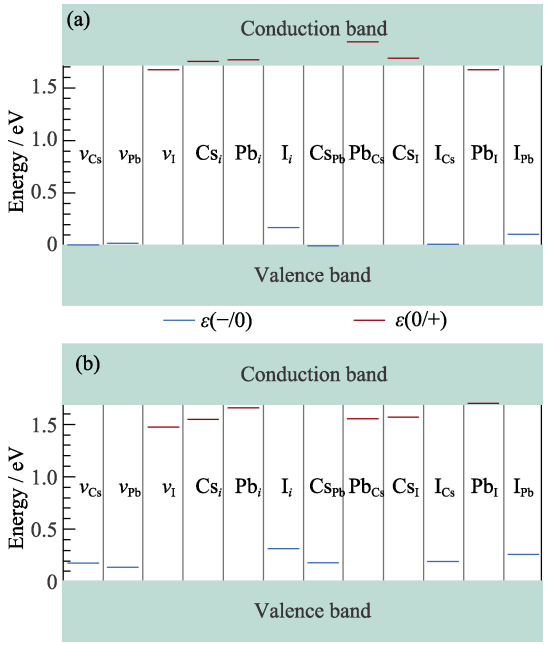

Fig. 4　Defect transition levels in γ-$CsPbI_3$ calculated by HSE-0.43 (a) and PBE0-0.2 (b)

Blue lines: acceptor levels; Red lines: donor levels

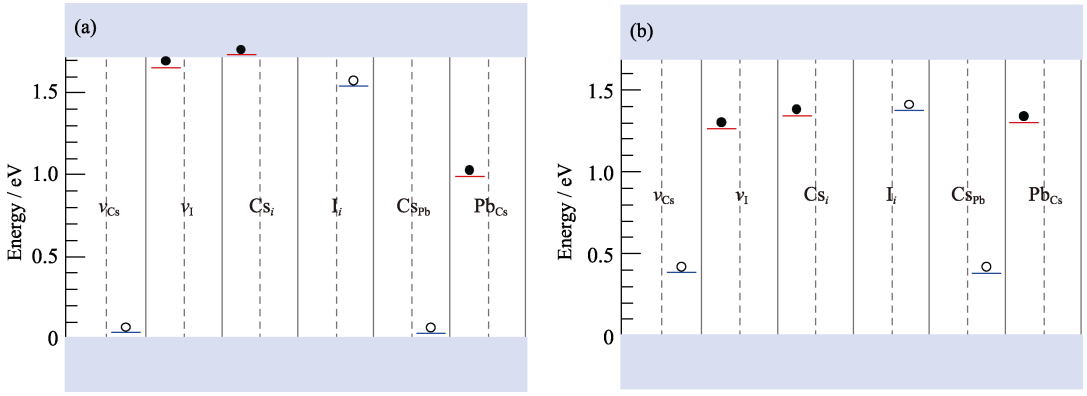

Fig. 5 Kohn-Sham energy levels of v_{Cs}, v_I, Cs_i, I_i, Cs_{Pb} and Pb_{Cs} defects calculated by HSE-0.43 (a) and PBE0-0.2 (b)
For acceptor defects, the left half is for −1 state, while the right half is for the neutral state. For donor defects, the left half is for neutral state, while the right half is for +1 state. Open and solid circles represent holes and electrons, respectively.

of above four defects clearly enter the band gap, which is consistent with the appearance of deep DTL in Fig. 4(b).

The cases of I_i and Pb_{Cs} are more complicated. Previous studies have shown that I_i may have both acceptor and donor properties (*i.e.* amphoteric defect)[54]. The structural distortions of both defects are relatively large, which may lead to the appearance of deep-level defects. Both functionals in Fig. 4 give a deeper $\varepsilon(-/0)$ level for I_i, and the result from PBE0-0.2 is slightly deeper. For the $\varepsilon(0/+)$ level of Pb_{Cs}, the result from HSE-0.43 is above CBM, indicating that the level is relatively shallow, while the result from PBE0-0.2 is deeper as shown in Fig. 4(b). Although the Kohn-Sham levels of Pb_{Cs} in Fig. 5 are deep, its $\varepsilon(0/+)$ level is not a deep-level defect, which is related to the detailed bonding situation of Pb at Cs site.

Comparing the results of two functionals, it is found that, relative to PBE0-0.2, although the proportion of Hartree-Fock exchange in HSE-0.43 is higher, it still gives correct results for typical shallow-level defects. The exchange interaction in Hartree-Fock calculations is a long-range interaction. In supercell calculations, the size of the supercell is usually not sufficient to avoid the interaction between the defect and its periodic images, which leads to a decrease in the energy level of the defect and its entry into the bandgap. This is the reason for the deep-level defects observed in PBE0-0.2[55]. In contrast, HSE-0.43 screens the long-range Hartree-Fock interaction and can avoid this problem even in a relatively small supercell of 160 atoms, as used in this study. In principle, PBE0-0.2 may also obtain shallower levels in larger supercells.

3 Conclusions

This study compared the performance of two main hybrid functional methods, HSE-0.43 and PBE0-0.2, in calculating the intrinsic defect properties of the orthorhombic phase $CsPbI_3$. To accurately describe the band gap, all defect calculations considered the spin-orbit coupling effect, including structural relaxation. The properties of the bulk phase were firstly studied using two methods, and it was found that except for slight quantitative differences, their results were basically consistent. However, there were qualitative differences between the defect transition energy levels and Kohn-Sham energy levels obtained by two methods. The shallow energy levels obtained by HSE-0.43 were mostly converted to deep energy levels in PBE0-0.2 calculations. This result is attributed to the long-range interaction of the Hartree-Fock exchange potential, which cannot be avoided in PBE0-0.2 calculations using small-size supercells, while the HSE functional, which screens the long-range Hartree-Fock exchange potential, could obtain the converged defect properties using relatively small supercells. Therefore, the HSE functional is an efficient method for accurate prediction of the defect properties of halide perovskite materials, and eligible for the related design of photovoltaic, light-emitting and scintillation materials.

Supporting materials

Supporting materials related to this article can be found at https://doi.org/10.15541/jim20220756.

References:

[1] LEE M M, TEUSCHER J, MIYASAKA T, *et al*. Efficient hybrid solar cells based on meso-superstructured organometal halide perovskites. *Science*, 2012, **338:** 643.
[2] BURSCHKA J, PELLET N, MOON S J, *et al*. Sequential deposition as a route to high-performance perovskite-sensitized solar cells. *Nature*, 2013, **499(7458):** 316.
[3] GREEN M A, HO-BAILLIE A, SNAITH H J. The emergence of perovskite solar cells. *Nature Photonics*, 2014, **8(7):** 506.
[4] JEON N J, NOH J H, YANG W S, *et al*. Compositional

engineering of perovskite materials for high-performance solar cells. *Nature*, 2015, **517(7535):** 476.

[5] SALIBA M, MATSUI T, DOMANSKI K, *et al*. Incorporation of rubidium cations into perovskite solar cells improves photovoltaic performance. *Science*, 2016, **354(6309):** 206.

[6] MCMEEKIN D P, SADOUGHI G, REHMAN W, *et al*. A mixed-cation lead mixed-halide perovskite absorber for tandem solar cells. *Science* 2016, **351(6269):** 151.

[7] KOJIMA A, TESHIMA K, SHIRAI Y, *et al*. Organometal halide perovskites as visible-light sensitizers for photovoltaic cells. *Journal of the American Chemical Society*, 2009, **131:** 6050.

[8] LIU M, JOHNSTON M B, SNAITH H J. Efficient planar heterojunction perovskite solar cells by vapour deposition. *Nature*, 2013, **501(7467):** 395.

[9] NREL. Best research-cell efficiency chart[2023-04-05]. https://www.nrel.gov/pv/cell-efficiency.html.

[10] BELIKOVICH B A, PASHCHUK I P, PIDZYRAILO N S. Luminescence of $CsPbCl_3$ single-crystals. *Optikai I Spectroskopiya*, 1977, **42:** 113.

[11] ERA M, MORIMOTO S, TSUTSUI T, *et al*. Organic-inorganic heterostructure electroluminescent device using a layered perovskite semiconductor $(C_6H_5C_2H_4NH_3)_2PbI_4$. *Applied Physics Letters*, 1994, **65(6):** 676.

[12] TAN Z K, MOGHADDAM R S, LAI M L, *et al*. Bright light-emitting diodes based on organometal halide perovskite. *Nature Nanotechnology*, 2014, **9(9):** 687.

[13] LIN K, XING J, QUAN L N, *et al*. Perovskite light-emitting diodes with external quantum efficiency exceeding 20 percent. *Nature*, 2018, **562(7726):** 245.

[14] CAO Y, WANG N, TIAN H, *et al*. Perovskite light-emitting diodes based on spontaneously formed submicrometre-scale structures. *Nature*, 2018, **562(7726):** 249.

[15] STRANKS S D, SNAITH H J. Metal-halide perovskites for photovoltaic and light-emitting devices. *Nature Nanotechnology*, 2015, **10(5):** 391.

[16] FANG Y, DONG Q, SHAO Y, *et al*. Highly narrowband perovskite single-crystal photodetectors enabled by surface-charge recombination. *Nature Photonics*, 2015, **9(10):** 679.

[17] DOU L, YANG Y M, YOU J, *et al*. Solution-processed hybrid perovskite photodetectors with high detectivity. *Nature Communications*, 2014, **5:** 5404.

[18] YIN W J, SHI T, YAN Y. Unusual defect physics in $CH_3NH_3Pb_3$ perovskite solar cell absorber. *Applied Physics Letters*, 2014, **104(6):** 063903.

[19] YIN W, SHI T, YAN Y. Unique properties of halide perovskites as possible origins of the superior solar cell performance. *Advanced Materials*, 2014, **26(27):** 4653.

[20] BRANDT R E, STEVANOVIĆ V, GINLEY D S, *et al*. Identifying defect-tolerant semiconductors with high minority-carrier lifetimes: beyond hybrid lead halide perovskites. *MRS Communications*, 2015, **5(2):** 265.

[21] MEGGIOLARO D, MOTTI S G, MOSCONI E, *et al*. Iodine chemistry determines the defect tolerance of lead-halide perovskites. *Energy and Environmental Science*, 2018, **11(3):** 702.

[22] KURCHIN R C, GORAI P, BUONASSISI T, *et al*. Structural and chemical features giving rise to defect tolerance of binary semiconductors. *Chemistry of Materials*, 2018, **30(16):** 5583.

[23] PARK J S, KIM S, XIE Z, *et al*. Point defect engineering in thin-film solar cells. *Nature Reviews Materials*, 2018, **3(7):** 194.

[24] KANG J, WANG L. High defect tolerance in lead halide perovskite $CsPbBr_3$. *The Journal of Physical Chemistry Letters*, 2017, **8:** 489.

[25] MING C, WANG H, WEST D, *et al*. Defect tolerance in $CsPbI_3$: reconstruction of potential energy landscape and band degeneracy in spin-orbit coupling. *Journal of Materials Chemistry A*, 2022, **10(6):** 3018.

[26] AGIORGOUSIS M L, SUN Y Y, ZENG H, *et al*. Strong covalency-induced recombination centers in perovskite solar cell material $CH_3NH_3PbI_3$. *Journal of the American Chemical Society*, 2014, **136(41):** 14570.

[27] WU X W, MING C, SHI J, *et al*. Defects in statically unstable solids: the case for cubic perovskite α-$CsPbI_3$. *Chinese Physics Letters*, 2022, **39(4):** 046101.

[28] NEUKIRCH A J, NIE W, BLANCON J C, *et al*. Polaron stabilization by cooperative lattice distortion and cation rotations in hybrid perovskite materials. *Nano Letters*, 2016, **16(6):** 3809.

[29] GAO Y, LUO T, XIA Y, *et al*. The joint effect of spin-orbit coupling and atomistic disorder on bandgap evolution in inorganic $CsSn_{1-x}Pb_xI_3$ mixed perovskite. *Journal of Applied Physics*, 2022, **131(5):** 055107 .

[30] MOSCONI E, MERABET B, MEGGIOLARO D, *et al*. First-principles modeling of bismuth doping in the $MAPbI_3$ perovskite. *Journal of Physical Chemistry C*, 2018, **122(25):** 14107.

[31] BISCHOFF T, WIKTOR J, CHEN W, *et al*. Nonempirical hybrid functionals for band gaps of inorganic metal-halide perovskites. *Physical Review Materials*, 2019, **3(12):** 123802.

[32] TAO S, SCHMIDT I, BROCKS G, *et al*. Absolute energy level positions in tin- and lead-based halide perovskites. *Nature Communications*, 2019, **10:** 2560.

[33] MAHATA A, MEGGIOLARO D, DE ANGELIS F. From large to small polarons in lead, tin, and mixed lead-tin halide perovskites. *Journal of Physical Chemistry Letters*, 2019, **10(8):** 1790.

[34] WANG J, ZHANG J, ZHOU Y, *et al*. Highly efficient all-inorganic perovskite solar cells with suppressed non-radiative recombination by a lewis base. *Nature Communications*, 2020, **11:** 177.

[35] LIU C, IGCI C, YANG Y, *et al*. Dopant-free hole transport materials afford efficient and stable inorganic perovskite solar cells and modules. *Angewandte Chemie International Edition*, 2021, **60(37):** 20489.

[36] KAISER W, CARIGNANO M, ALOTHMAN A A, *et al*. First-principles molecular dynamics in metal-halide perovskites**:** contrasting generalized gradient approximation and hybrid functionals. *Journal of Physical Chemistry Letters*, 2021, **12(49):** 11886.

[37] VONA C, NABOK D, DRAXL C. Electronic structure of (organic-)inorganic metal halide perovskites: the dilemma of choosing the right functional. *Advanced Theory and Simulations*, 2022, **5(1):** 2100496.

[38] MEGGIOLARO D, DE ANGELIS F. First-principles modeling of defects in lead halide perovskites: best practices and open issues. *ACS Energy Letters*, 2018, **3(9):** 2206.

[39] EPERON G E, PATERNÒ G M, SUTTON R J, *et al*. Inorganic caesium lead iodide perovskite solar cells. *Journal of Materials Chemistry A*, 2015, **3(39):** 19688.

[40] SWARNKAR A, MARSHALL A R, SANEHIRA E M, *et al*. Quantum dot-induced phase stabilization of α-$CsPbI_3$ perovskite for high-efficiency photovoltaics. *Science*, 2016, **354(6308):** 92.

[41] YOON S M, MIN H, KIM J B, *et al*. Surface engineering of ambient-air-processed cesium lead triiodide layers for efficient solar cells. *Joule*, 2021, **5:** 183.

[42] WANG P, ZHANG X, ZHOU Y, *et al*. Solvent-controlled growth of inorganic perovskite films in dry environment for efficient and stable solar cells. *Nature Communications*, 2018, **9:** 2225.

[43] WANG Y, DAR M I, ONO L K, *et al*. Thermodynamically

stabilized β-$CsPbI_3$-based perovskite solar cells with efficiencies > 18%. *Science*, 2019, **365(6453):** 591.
[44] ZHAO B, JIN S F, HUANG S, *et al*. Thermodynamically stable orthorhombic γ-$CsPbI_3$ thin films for high-performance photovoltaics. *Journal of the American Chemical Society*, 2018, **140(37):** 11716.
[45] WANG K, JIN Z, LIANG L, *et al*. Chlorine doping for black γ-$CsPbI_3$ solar cells with stabilized efficiency beyond 16%. *Nano Energy* 2019, **58:** 175.
[46] LI Z, YANG M, PARK J S, *et al*. Stabilizing perovskite structures by tuning tolerance factor: formation of formamidinium and cesium lead iodide solid-state alloys. *Chemistry of Materials*, 2016, **28(1):** 284.
[47] WANG Y, CHEN Y, ZHANG T, *et al*. Chemically stable black phase $CsPbI_3$ inorganic perovskites for high-efficiency photovoltaics. *Advanced Materials*, 2020, **32(45):** 2001025.
[48] XIANG W, LIU S, TRESS W, *et al*. A review on the stability of inorganic metal halide perovskites: challenges and opportunities for stable solar cells. *Energy & Environmental Science*, 2021, **14(4):** 2090.
[49] CUI Y, SHI J, MENG F, *et al*. A versatile molten-salt induction strategy to achieve efficient $CsPbI_3$ perovskite solar cells with a high open-circuit voltage >1.2 V. *Advanced Materials*, 2022, **34(45):** 2205028.
[50] KRESSE G, FURTHMÜLLER J. Efficiency of *ab-initio* total energy calculations for metals and semiconductors using a plane-wave basis set. *Computational Materials Science*, 1996, **6:** 15.
[51] BLÖCHL, P. E. Projector augmented-wave method. *Physical Review B*, 1994, **50(24):** 17953.
[52] KRESSE G, JOUBERT D. From ultrasoft pseudopotentials to the projector augmented-wave method. *Physical Review B*, 1999, **59:** 1758.
[53] WU X W, GAO W, CHAI J, *et al*. Defect tolerance in chalcogenide perovskite photovoltaic material $BaZrS_3$. *Science China Materials*, 2021, **64(12):** 2976.
[54] ZHANG X, TURIANSKY M E, SHEN J X, *et al*. Iodine interstitials as a cause of nonradiative recombination in hybrid perovskites. *Physical Review B*, 2020, **101(14):** 140101(R).
[55] BANG J, SUN Y Y, ABTEW T A, *et al*. Difficulty in predicting shallow defects with hybrid functionals: implication of the long-range exchange interaction. *Physical Review B*, 2013, **88(3):** 035134.

杂化泛函 HSE 和 PBE0 计算 $CsPbI_3$ 缺陷性质的比较研究

吴晓维[1], 张 涵[1,2], 曾 彪[1,2], 明 辰[1,2], 孙宜阳[1,2]

(1. 中国科学院 上海硅酸盐研究所, 上海 201899; 2. 中国科学院大学 材料科学与光电工程中心, 北京 100049)

摘 要:在卤族钙钛矿材料的缺陷研究中, 密度泛函理论计算发挥着重要作用。传统的半局域泛函(如 PBE)虽然能够得到与实验接近的禁带宽度, 但是已有研究表明其不能准确描述材料的带边位置。采用更准确的杂化泛函, 结合自旋轨道耦合(SOC)效应与充分的结构优化开展缺陷研究十分必要。可以选择两种杂化泛函, 即屏蔽的杂化泛函 HSE 和非屏蔽的杂化泛函 PBE0。本研究以正交相 $CsPbI_3$ 为例, 系统比较了两种方法在缺陷性质计算上的差异。计算结果表明, 对于体相性质, 两种杂化泛函并无明显的差别。但是, 对于缺陷性质, 两种泛函出现定性的差别。HSE 计算中预测的浅能级缺陷, 在 PBE0 计算中大部分变为深能级缺陷, 且缺陷转变能级和 Kohn-Sham 能级均出现定性差别。上述差别的本质在于, Hartree-Fock 交换势具有长程作用特征, 因而普通的杂化泛函如 PBE0 在计算量允许的超胞尺寸上无法得到收敛的结果, 而 HSE 对上述交换势具有屏蔽作用, 可采用相对小尺寸的超胞得到收敛的缺陷能级。本研究结果表明, 尽管 HSE 杂化泛函需要较大的 Hartree-Fock 混合参数(约 0.43), 其仍是准确计算卤族钙钛矿缺陷性质的有效方法。

关 键 词: 钙钛矿; 本征缺陷; $CsPbI_3$; 杂化泛函; 第一性原理计算

中图分类号: TQ174 **文献标志码:** A

Supporting materials

Comparison of Hybrid Functionals HSE and PBE0 in Calculating the Defect Properties of $CsPbI_3$

WU Xiaowei[1], ZHANG Han[1,2], ZENG Biao[1,2], MING Chen[1,2], SUN Yiyang[1,2]

(1. Shanghai Institute of Ceramics, Chinese Academy of Sciences, Shanghai 201899, China; 2. Center of Materials Science and Optoelectronics Engineering, University of Chinese Academy of Sciences, Beijing 100049, China)

Fig. S1 compares the density of states (DOS) obtained by the two methods. It can be seen that, except for the smaller valence band width obtained by PBE0-0.2, there are no other significant differences. Each peak on two total DOS curves can be corresponded to each other, but the peak positions are slightly shifted. From the decomposed DOS curves, it can be seen that the valence band is mainly contributed by the p orbitals of I, and the s orbitals of Pb also contribute near the valence band maximum (VBM). The conduction band minimum (CBM) is mainly contributed by the p orbitals of Pb.

Fig. S2 compares the effective masses of carriers obtained by two methods through parabolic fitting. CBM and VBM are taken as the energy reference points for the conduction and valence bands, respectively, for convenience of plotting. It can be seen that the energy bands near the Γ point can be well fitted by parabolas along three principal axes directions. The maximum difference in effective mass along three directions is about $0.1m_0$. The difference in effective masses of electrons and holes is also small, indicating a balanced electron-hole transport property of $CsPbI_3$.

Fig. S3 shows the real and imaginary parts of the dielectric constant, respectively. Since the accurate calculation of dielectric constant requires a sufficient number of empty states and a sufficient high density of *k*-points, the PBE functional was first employed to test the convergence of the number of empty states and the

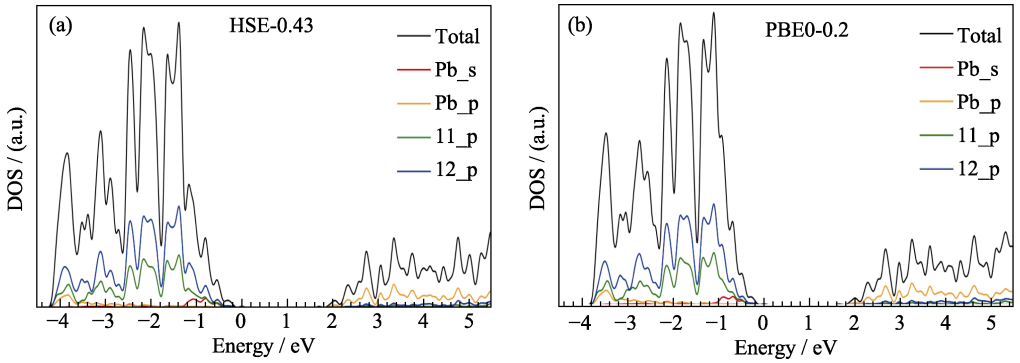

Fig. S1　Total and projected density of states of γ-$CsPbI_3$ calculated by two hybrid functionals HSE-0.43 (a) and PBE0- 0.2 (b) including the SOC effect

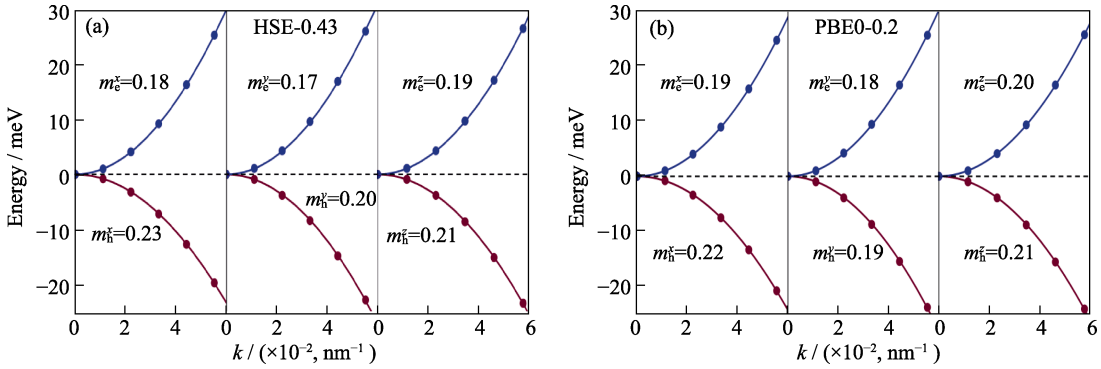

Fig. S2　Parabolic fitting of the band near Γ point to obtained the effective masses of electrons and holes. For clarity, the electron and hole bands are referenced to the CBM and VBM, respectively; SOC effect is included here; (a) HSE-0.43; (b) PBE0-0.2

density of *k*-points. The results showed that a 5×4×5 *k*-point grid and 544 empty states can converge the calculated dielectric constant to an accuracy of about 0.01. Figure S3 shows that there is a slight difference in the bulk dielectric constant calculated by the HSE-0.43 and PBE0-0.2 functionals. The difference is about 0.19 for ε_1 at 0 eV and the slight lagging behind of ε_2 calculated by HSE-0.43 is related to the slightly wider band gap obtained by this method.

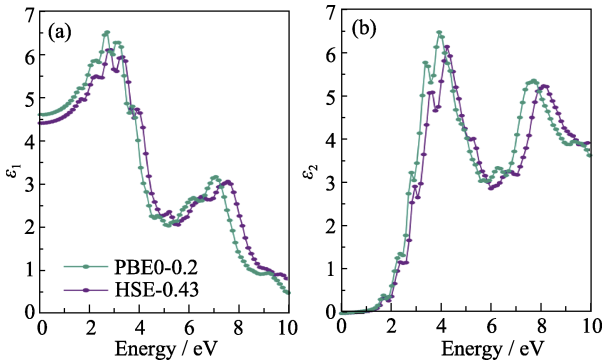

Fig. S3 Comparison of dielectric constants calculated by two hybrid functionals

(a) Real part ε_1; (b) Imaginary part ε_2; Calculations considered SOC effect and employed 5×4×5 *k*-grid and 544 empty bands